
STRUC2MAPGAN: IMPROVING SYNTHETIC CRYO-EM DENSITY MAPS WITH GENERATIVE ADVERSARIAL NETWORKS

Chenwei Zhang¹Anne Condon¹Khanh Dao Duc²¹ Department of Computer Science, UBC
{cwzhang, condon}@cs.ubc.ca² Department of Mathematics, UBC
kdd@math.ubc.ca

ABSTRACT

Generating synthetic cryogenic electron microscopy 3D density maps from molecular structures has potential important applications in structural biology. Yet existing simulation-based methods cannot mimic all the complex features present in experimental maps, such as secondary structure elements. As an alternative, we propose *struc2mapGAN*, a novel data-driven method that employs a generative adversarial network to produce improved experimental-like density maps from molecular structures. More specifically, *struc2mapGAN* uses a nested U-Net architecture as the generator, with an additional L1 loss term and further processing of raw training experimental maps to enhance learning efficiency. While *struc2mapGAN* can promptly generate maps after training, we demonstrate that it outperforms existing simulation-based methods for a wide array of tested maps and across various evaluation metrics.

1 Introduction

Cryogenic electron microscopy (cryo-EM) is a powerful technique for structural determination of biological macromolecules such as proteins and nucleic acids, which has been widely used in structure-based drug discovery [1, 2]. Cryo-EM produces a series of 2D images that are then reconstructed into electron density maps, providing a 3D voxelized representation of the macromolecular complex.

For the past few years, deep learning-based methods have been introduced to automate the construction of macromolecular atomic models from density maps (i.e. 3D coordinate structure) [3, 4, 5]. However, most of these methods require high-fidelity experimental maps, given the lack of reliable experimentally derived map-model pairs at lower resolutions [6]. In this context, generating accurate synthetic maps can help to include the vast majority of structures that are limited to be solved at lower resolutions. In addition, these can also be used for “rigid-body fitting” in the building process (i.e. aligning a whole or partial atomic model into a density map [7, 8]), “sharpening” density maps [9, 10] (i.e. enhancing the map to facilitate model building) [5], or providing more ground-truth training targets.

As generating synthetic cryo-EM density maps has become a pivot, various simulation-based methods are available [8, 11, 12, 13, 14], essentially using a resolution-lowering point spread function to convolute atom points extracted from PDB structures (atomic models). Upon treating atoms independently, these methods may fail to characterize more complex features, such as secondary structure elements (SSEs), interatomic interactions, or specific image artifacts inherent to the 3D reconstruction process. In addition, Alshammari et al. [15] proposed an approach to generate cryo-EM maps by applying a Gaussian convolution to an experimental map rather than deriving from an atomic structure, allowing for the capture of complex features. As an alternative, we thus introduce a data-driven approach that leverages generative models. Our method, called *struc2mapGAN*, uses a generative adversarial network (GAN) to enhance the generation of experimental-like cryo-EM density maps from PDB structures. Our contributions are as follows.

- We introduce the first deep learning-based method, to our knowledge, for generative modeling of cryo-EM density maps. Our method enhances the learning efficiency by curating high-quality training data and alleviates mode collapse [16] in GANs through the integration of SmoothL1Loss into the model.

- Our benchmarking shows superior overall performance against simulation-based methods, across various evaluation metrics (e.g. correlation) and over a variety of tested maps. Our experiments also suggest that this performance improvement results from better capture of SSEs.
- We benchmark the runtime of *struc2mapGAN* and demonstrate its practical suitability for generating large-scale maps.

2 Related work

2.1 Existing simulation-based methods

Simulation-based methods for generating density maps from their associated PDB structures are based on the convolution of atom points with resolution-lowering point spread functions such as Gaussian, triangular, or hard-sphere [17, 18]. Given a PDB structure containing M atoms, a general Gaussian simulation formula for producing a density value ρ at a grid point \mathbf{x} is expressed as:

$$\rho(\mathbf{x}) = \sum_{i=1}^M \theta Z_i e^{-k|\mathbf{x}-\mathbf{r}_i|^2}, \quad (1)$$

where Z_i represents the atomic number and \mathbf{r}_i is the position vector of the i -th heavy atom, θ is a scaling factor and k is defined in terms of the resolution [9, 5]. Such methods including *e2pdb2mrc* in EMAN2 [11] (originally called *pdb2mrc* in EMAN1 [8]), *molmap* in UCSF ChimeraX [12], *StructureBlurrer* in TEMPy2 [13], and *pdb2vol* in Situs [14], generate 3D density maps using a Gaussian point spread function, where the real-space dimension corresponds to the desired resolution, which varies based on the specific resolution convention of each package.

2.2 Generative adversarial networks

GAN is one of the most prevalent generative models widely employed in image generation, super-resolution, and 3D object generation [19]. The GAN architecture comprises two main models, a generator G and a discriminator D trained together. G generates a batch of images (we call them fake images), and these images are fed along real images (ground-truth reference images) into D to be classified as real or fake. During training, G generates fake images to fool D , while D is updating its parameters to discriminate the fake ones. Mathematically speaking, the two models G and D compete in a two-player minimax game with the objective function $L(G, D)$:

$$\min_G \max_D V(D, G) = \mathbb{E}_{\mathbf{x}}[\log D(\mathbf{x})] + \mathbb{E}_{\mathbf{z}}[\log(1 - D(G(\mathbf{z})))] \quad (2)$$

The generator minimizes the $\log(1 - D(G(\mathbf{z})))$ term predicted by D for fake images. Conversely, the discriminator maximizes the log probability of real images, $\log D(\mathbf{x})$ and the log probability of correctly identifying fake images, $\log(1 - D(G(\mathbf{z})))$. Over the past few years, the GAN architecture has been adapted for various purposes and has demonstrated superior performance in multiple domains [20, 21, 22, 23, 24].

3 Materials and Methods

3.1 Datasets

Training and validation data: To train and validate the GAN model, our dataset was built with a set of high-resolution cryo-EM density maps ranging from 2.17 Å to 3.9 Å from the EMDB databank [25] and associated PDB structures from the PDB databank [26]. To ensure the density maps have proper alignments with their associated PDB structures, we removed maps from the dataset if: (i) maps contain extensive regions without corresponding PDB structures; (ii) maps are misaligned with associated PDB structures; (iii) maps contain various macromolecules, such as nucleic acids; (iv) PDB structures only contain backbone atoms and/or include unknown residues. In addition, pairs of simulated and experimental maps with correlation lower than 0.65 (calculated using ChimeraX) were excluded. To eliminate data redundancy, we measured the sequence identity between PDB structures and retained only one when the identity exceeded 30 %. After applying these filtering steps, a total of 149 cryo-EM density maps and associated PDB structures remained, as listed in Supplementary Table S1. 134 map-PDB pairs (90 %) were selected as the training set and 15 pairs (10 %) as the validation set.

Test data: For the test set, we randomly selected 130 PDB structures from the PDB databank and associated cryo-EM density maps from the EMDB databank with resolution ranging from 3 Å to 7.9 Å, as detailed in Supplementary Table S2. Note that these 130 examples do not overlap with the training and validation data sets.

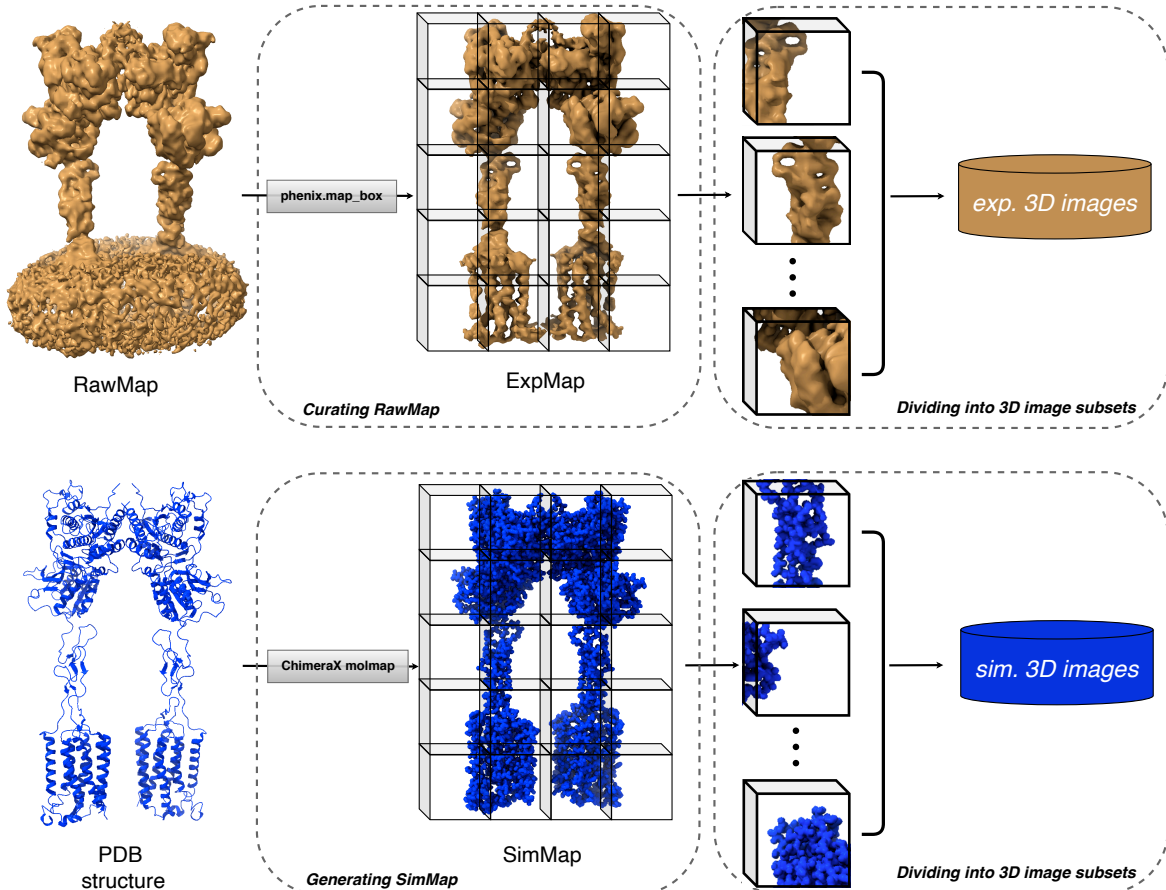


Figure 1: The data preprocessing workflow. The top panel depicts the process of curating raw experimental maps and dividing the curated maps into 3D image subsets as training targets. The bottom panel depicts the process of generating simulated maps and dividing them into 3D image subsets as training inputs.

3.2 Preprocessing:

According to the following preprocessing steps illustrated in Figure 1, both experimental maps (denoted as *RawMaps*) and simulated maps from PDB structures (denoted as *SimMaps*) were pre-processed to facilitate the GAN training. In addition, our GAN architecture also takes 3D images of reduced size as input.

Curating RawMaps: The raw experimental maps consistently contain background noise, such as lipid solvents and artifacts from nanodiscs, which compromise the pairing accuracy between *RawMaps* and *SimMaps*. To mitigate these effects, we applied a mask to the raw map to isolate the region containing only the protein structure. We first aligned the PDB structure with the corresponding map and employed *phenix.map_box* to create a rectangular box slightly larger than the targeted region. Subsequently, we resampled the masked map at a grid voxel size of $1\text{\AA} \times 1\text{\AA} \times 1\text{\AA}$ and applied min-max normalization to scale the map’s voxel values to the range of $[0, 1]$ to maintain uniformity. The curated map, termed *ExpMap*, was then employed for training the network. Note that this curation strategy to make *ExpMap* targets significantly enhanced the performance of the GAN model, as evidenced in our ablation study (see section 5).

Generating SimMaps: The input data *SimMaps* were simulated using the *molmap* function. We converted the PDB structure into a simulated density map on a grid corresponding to the *ExpMap*, with a resolution cutoff at 2\AA . This simulated map was then min-max normalized to the range of $[0, 1]$, aligning with its corresponding *ExpMap*. Moreover, in light of enhancing the model’s robustness, we utilized *TorchIO* [27] to add random Gaussian noise, random anisotropy, and random blur to augment the input data.

Dividing maps into 3D image subsets: Considering the varying dimensions of each map and the constraints of GPU memory, we zero-padded the *SimMaps* and *ExpMaps* and divided them into smaller 3D images (denoted as *exp. 3D images* and *sim. 3D images*, respectively) with dimensions of $32 \times 32 \times 32$. To do so, we first created a padded map that exceeded the dimensions of the input map by 2×32 in each dimension, ensuring no boundary issues. The original map was then centrally placed within this padded map. Following this procedure yielded a total of 403710 3D images for training and 62635 for validation.

3.3 The GAN architecture

Figure 2 depicts the *struc2mapGAN* architecture that comprises a generator and a discriminator. We have implemented a nested U-Net architecture (U-Net++) [28] as the generator (shown in the bottom panel of Figure 2). The encoder and decoder blocks of the U-Net++ follow the same design, each consisting of 3D convolution layers with a kernel size of $3 \times 3 \times 3$. Unlike standard U-Nets, U-Net++ applies dense skip connections that effectively bridge the encoder and decoder feature maps, for enhanced gradient flow. 3D max-pooling layers, featuring a kernel size of 2 and a stride of 2, are employed for down-sampling, while trilinear interpolation layers with a scale factor of 2 are used for up-sampling.

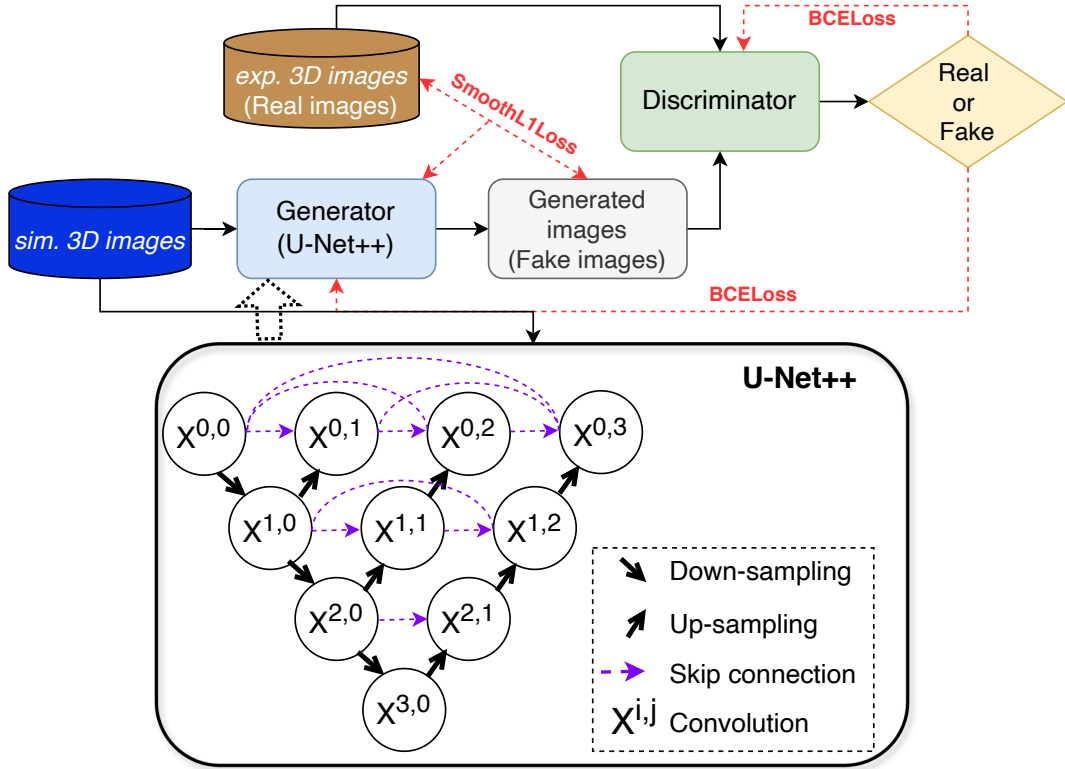


Figure 2: The *struc2mapGAN* architecture. The bottom panel illustrates the U-Net++ architecture. $X^{i,j}$ refers to the convolution block at depth i and position j of the network.

The discriminator network has been designed for 3D volumetric data classification. It consists of four 3D convolution layers with a kernel size of $3 \times 3 \times 3$. An adaptive average-pooling layer is applied after the last convolution layer to reduce the feature map to the size of $1 \times 1 \times 1$, which is then flattened and passed through three fully connected layers with ReLU activations between them. The final layer outputs a single value for binary classification.

For both the generator and discriminator, we employed a parametric rectified linear unit (PReLU) as the activation function between convolution layers, coupled with instance normalization. We opted for instance normalization over the more commonly used batch normalization as the statistics should not be averaged across instances within a batch. This consideration is crucial since local 3D image subsets of cryo-EM density may originate from different maps. The total number of parameters for the generator is 10.3 million and for the discriminator is 1.2 million.

3.4 Training and inference of struc2mapGAN

Training: During training, *struc2mapGAN* accepts paired *sim. 3D images* and *exp. 3D images* as input and outputs modified images. To impose the generator to minimize the difference between the prediction and the target, we incorporated the standard adversarial loss for each input *sim. 3D image* with the smooth L1 loss in the generator, as

$$\text{SmoothL1Loss}(X, Y) = \begin{cases} 0.5(X - Y)^2, & \text{if } |X - Y| < 1, \\ |X - Y| - 0.5, & \text{otherwise,} \end{cases} \quad (3)$$

where X is the GAN-predicted image, i.e. $G(\text{sim. 3D image})$, and Y is the paired target image, i.e. *exp. 3D image*. The adversarial loss is calculated as the binary cross entropy loss of the discriminator’s predictions, as

$$\text{Loss}_{\text{adversarial}} = -\log(D(X)). \quad (4)$$

Therefore, the generator loss is formulated as a linear combination of adversarial loss and smooth L1 loss:

$$\text{Loss}_G = \text{SmoothL1Loss} + \alpha \times \text{Loss}_{\text{adversarial}}, \quad (5)$$

where α is a tuning hyperparameter. The discriminator loss adheres to the standard GAN loss formula, aiming to classify X as fake and Y as real:

$$\text{Loss}_D = -(\log D(Y) + \log(1 - D(X))). \quad (6)$$

Inference: To generate a map from a PDB structure using our trained generator, the input PDB structure was initially converted to a map following the procedure of generating *SimMaps*. This converted map was subsequently zero-padded and divided into 3D image subsets with dimensions of $32 \times 32 \times 32$, following the same strategy employed during training data preprocessing. These image subsets were then refined by the trained generator to yield post-processed images. The post-processed images were then reassembled back to their original map dimensions. To ensure that no spatial information was lost, we exclusively utilized the center $20 \times 20 \times 20$ voxels of each 3D image to reconstruct the map, in accordance with the method proposed by Si et al. [29].

Implementation: *Struc2mapGAN* was implemented in PyTorch-2.2.2 + cuda-12.1, with all training and validating processes carried out on eight NVIDIA A100 GPUs, each with 80 GB VRAM. This setup supported a batch size of 128. The network was trained over 150 epochs, with each epoch taking approximately 765 seconds. The total training duration was approximately 1 day and 8 hours. For optimization, NAdam [30] optimizers were employed with a learning rate set at 0.0001. We tested three different α values: 0.1, 0.01, 0.001. Ultimately, $\alpha = 0.01$ was selected for yielding the best performance.

3.5 Evaluation metrics

To measure the accuracy of *struc2mapGAN* in generating maps that are similar to experimental reference ones, we used the following evaluation metrics.

Structural similarity index measure: The structural similarity index measure (SSIM) evaluates the similarity between two images based on three key features: luminance, contrast, and structure [31]. This measure has been extended to evaluate 3D volumetric data and has been adapted as a loss function in cryo-EM density map studies [9, 5]. The SSIM score between samples X and Y is calculated as follows:

$$\text{SSIM}(X, Y) = \frac{(2\mu_X\mu_Y + c_1)(2\sigma_{XY} + c_2)}{(\mu_X^2 + \mu_Y^2 + c_1)(\sigma_X^2 + \sigma_Y^2 + c_2)}, \quad (7)$$

where μ_X and μ_Y , σ_X and σ_Y are the means and variances of samples X and Y , respectively. σ_{XY} refers to the covariance of X and Y . Constants c_1 and c_2 are included to stabilize the division. SSIM excels in capturing the local contrast and textures, which are crucial in cryo-EM density maps. In our study, we employed the *scikit-image* package to calculate the SSIM between a *struc2mapGAN*-generated or simulation-based density map and its corresponding experimental map.

ChimeraX correlation: UCSF ChimeraX [12] provides a built-in *measure correlation* function to calculate the correlation between two density maps in two ways. One way is to compute the correlation between two maps directly without considering the deviations from their means:

$$\text{correlation}(X, Y) = \frac{\langle X, Y \rangle}{\|X\| \|Y\|}, \quad (8)$$

where $\langle X, Y \rangle$ represents the dot product of maps X and Y ; $\|X\| \|Y\|$ are the norms of the maps. The other way calculates the correlation between deviations of two maps from their means:

$$\text{correlation about mean}(X, Y) = \frac{\langle X - X_{\text{ave}}, Y - Y_{\text{ave}} \rangle}{\|X - X_{\text{ave}}\| \|Y - Y_{\text{ave}}\|}, \quad (9)$$

where X_{ave} and Y_{ave} are the means of the two maps. In the context of comparing cryo-EM density maps, we calculated the two correlations to assess the similarity across the entire volume of the two maps.

Pearson correlation coefficient: The Pearson correlation coefficient (PCC) is a measure of the linear correlation between two datasets [32] and is defined by:

$$\text{PCC}(X, Y) = \frac{\sum_{i=1}^n (X_i - \bar{X})(Y_i - \bar{Y})}{\sqrt{\sum_{i=1}^n (X_i - \bar{X})^2 \sum_{i=1}^n (Y_i - \bar{Y})^2}}, \quad (10)$$

where X_i and Y_i represent the individual data points in datasets X and Y , respectively. \bar{X} and \bar{Y} are the means of the datasets, and n is the total number of data points. In the context of comparing cryo-EM density maps, the PCC provides similarities between the two maps in terms of their density distributions.

4 Results

We conducted a comprehensive study to evaluate the performance of *struc2mapGAN* using a test set of 130 PDB structures and associated experimental density maps (note that these structures and maps were not used for training the GAN network). In our benchmarking, simulation-based maps were generated using various methods (*molmap*, *e2pdb2mrc*, and *StructureBlurrer*), with a resolution cutoff at 2 Å.

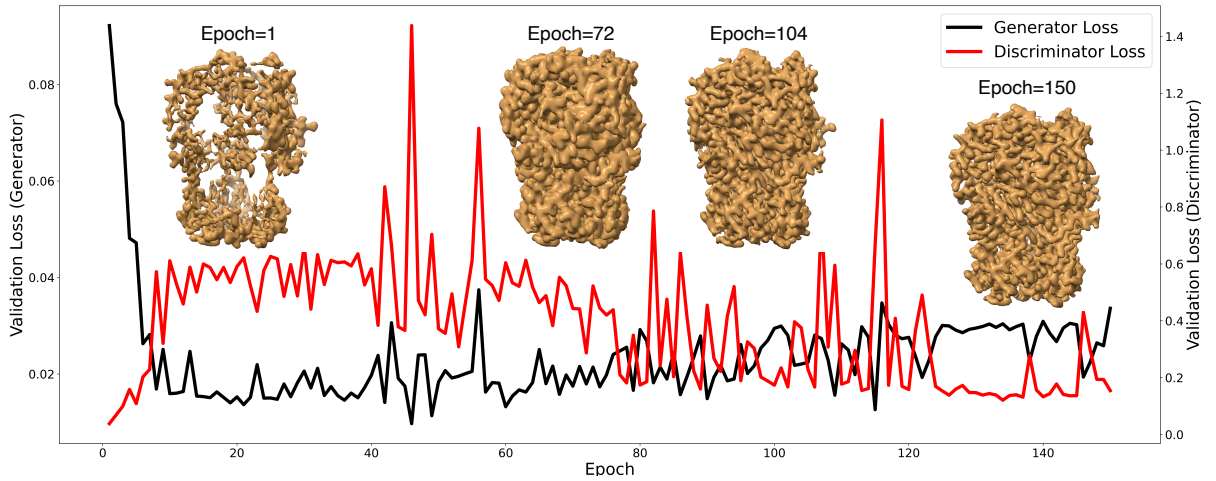


Figure 3: Validation loss curves of the generator and discriminator in black and red, respectively, with snapshots of generated maps from the models trained at specific epochs.

4.1 Learning curves with intermediate maps

To analyze the training process, we visualized the training dynamics of *struc2mapGAN* in Figure 3. The validation losses of both the generator (black) and discriminator (red) were plotted over 150 epochs. At the beginning of training, the generator loss decreased sharply, reflecting its quick adaptation to produce more realistic maps, while the discriminator loss slightly increased owing to the generator’s enhancements. Throughout the training, fluctuations in both losses indicate continuous learning and adaptation. By the end of the training, the losses of both the generator and discriminator tended to converge, suggesting a balanced and stabilized adversarial training outcome. Alongside the loss curves, selected *struc2mapGAN*-generated maps from epochs 1, 72, 104, and 150 were displayed. These intermediate maps visually encapsulated the gradual improvement in the quality and fidelity of the generated maps. For instance, the map from Epoch 1 showed incomplete densities. As training proceeded, the generated maps learned to represent complete densities, with their resolution progressively refined, as illustrated in the maps from Epoch 72 to Epoch 150.

4.2 Visual comparison between generated maps by *struc2mapGAN* and *molmap*

Upon training, we first visualized three GAN-generated density maps alongside their associated *molmap*-generated maps, with corresponding experimental maps ranging from high to low resolutions. The visual comparisons are displayed in Figure 4. We observed that as *struc2mapGAN* is trained to represent high-resolution maps, the GAN-generated maps were produced with consistent detail level across the three examples, with high correlation scores (0.891, 0.967 and 0.935) with experimental maps. In contrast, *molmap*-generated maps displayed fine-grained resolution at the level of individual atoms (0.676, 0.619 and 0.653). In practice, these maps effectively captured the spatial distribution of atomic densities but did not seem to distinctly represent SSEs (see on-set panels in Figure 4). In contrast, *struc2mapGAN* seemed to better capture SSEs such as α -helices and β -sheets. For instance, for EMDB-35136 in Figure 4c, the GAN-generated maps distinctly revealed the densities of helical and sheet structures, indicating that our model effectively learned the complexity of experimental maps. These visual results demonstrate that the maps synthesized by *struc2mapGAN* improved representation of SSEs.

4.3 Quantitative comparison over resolution

We then studied how the GAN-generated maps from PDB structures compare against the corresponding experimental counterpart, and how a simulation-based method like *molmap* performs in comparison. For this section, we also aimed to consider the resolution of the experimental map (ranging from high (3 Å) to low (7.9 Å)), since GAN-generated maps aim to replicate the map features at high resolution. As depicted in Figure 5, over 95 % of GAN-generated maps achieved high correlation scores above 0.8, irrespective of their resolution. Surprisingly, this correlation was also constant on average across resolution levels (as shown by the fitted curve). A similar result was obtained using SSIM (see Methods). We hypothesize that the information loss in low-resolution maps, that would result in poor placement of atoms in the PDB structure, was compensated by incorporating high-resolution training data, leading to maintaining performance in low-resolution maps. To support this hypothesis, we performed the same comparison using *molmap*-simulated maps at both high resolution of 2 Å, and the same reported resolution as the experimental one. In Table 1, we report the mean and median correlation and SSIM scores that indicate better performance of GAN-generated maps. As expected, simulated maps at 2 Å showed poorer correlation and similarity as resolution decreases resulting from less the accurate atomic model (see Figure 5). Simulated maps at reported resolution would maintain constant correlation (compensating atom misplacement by a more diffuse kernel), but with less value than *struc2mapGAN*, and also a decreasing trend for SSIM, supporting that GAN-generated maps can compensate for the uncertainty of atomic positions in PDB structures generated at low resolution.

Table 1: Performance comparison of different methods.

Methods	SSIM		Correlation		Correlation about mean		PCC	
	Mean	Median	Mean	Median	Mean	Median	Mean	Median
struc2mapGAN	0.841	0.896	0.906	0.943	0.466	0.502	0.594	0.621
molmap	0.771	0.774	0.559	0.573	0.315	0.311	0.452	0.470
StructureBlurrer	0.764	0.771	0.603	0.620	0.335	0.334	0.475	0.499
e2pdb2mrc	0.848	0.896	0.613	0.649	0.322	0.325	0.483	0.519

4.4 Benchmarking

We further compared *struc2mapGAN* with other commonly used simulation-based methods, including *StructureBlurrer* and *e2pdb2mrc*, in terms of SSIM, correlation, and PCC scores across all 130 test examples. The mean and median values of these metrics are listed in Table 1. According to the box-and-whisker plots shown in Figure 6, maps generated by *struc2mapGAN* consistently produced higher scores in metrics of correlation, correlation about mean, and PCC compared to the other methods. Specifically, *struc2mapGAN* achieved an average correlation of 0.906 and a PCC of 0.594, significantly surpassing the other methods. Although *struc2mapGAN*’s average SSIM score was 0.841, slightly lower than *e2pdb2mrc*’s 0.848, it exhibited a narrower interquartile range, indicating more consistent results. The high SSIM scores achieved by *e2pdb2mrc* can be attributed to its effective preservation of local structural details. This preservation is facilitated by the method’s requirement to select a larger box size ($500\text{\AA} \times 500\text{\AA} \times 500\text{\AA}$) than the reference for successfully generating a density map. A larger box size encompasses more spatial context around the molecule, thereby retaining more local structural details. Aside from the the SSIM score for *e2pdb2mrc*, we also observe that all three simulation-based methods yield comparable results across all metrics showing their relative similarity.

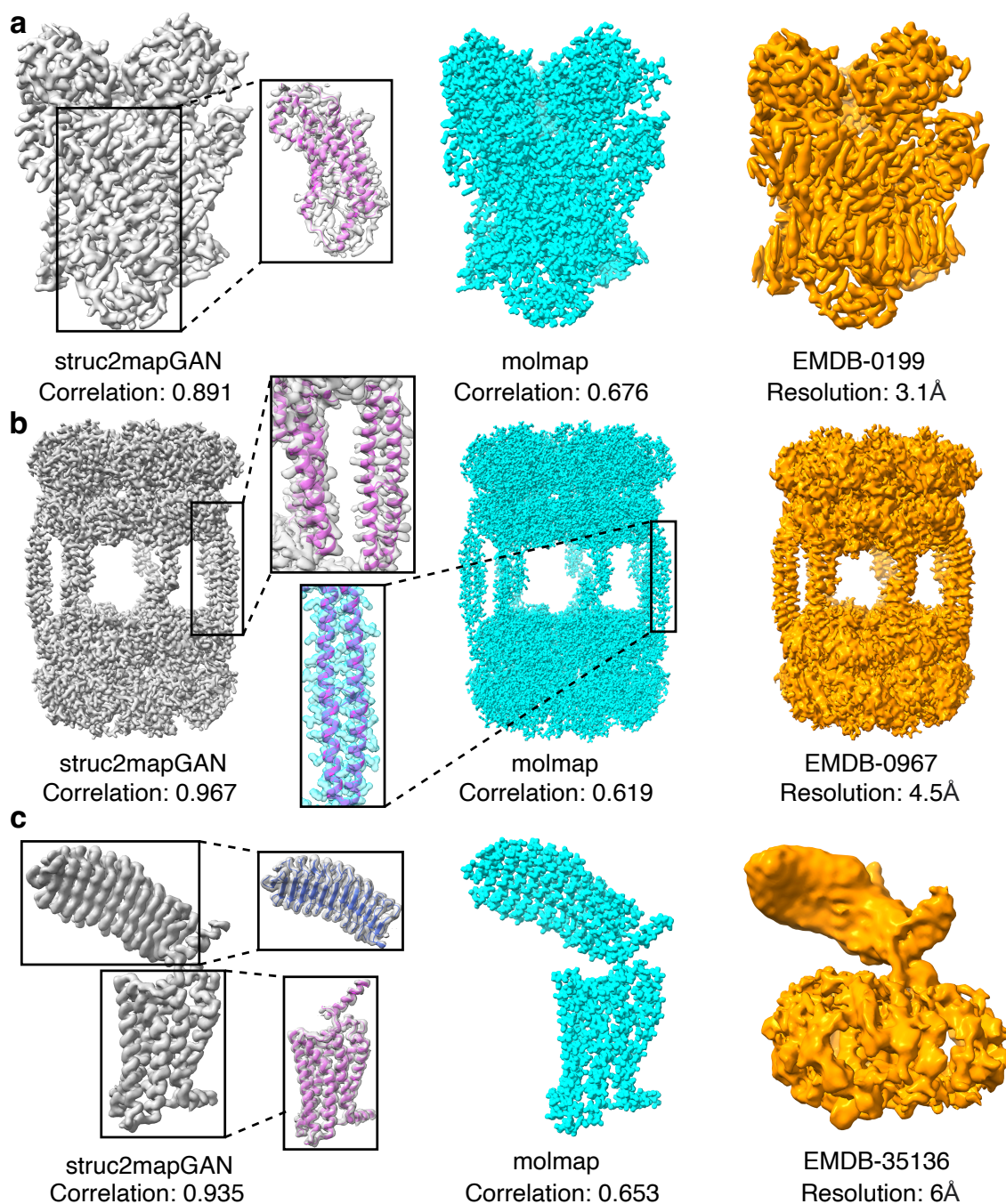


Figure 4: Examples of *struc2mapGAN* (gray) and *molmap* (cyan) generated maps, and the raw experimental maps (orange). The PDB structures of α -helices (pink) and β -sheets (blue) are superimposed on the maps. **a.** Human STEAP4 bound to NADP, FAD, heme and Fe(III)-NTA (EMDB ID: 0199; PDB ID: 6HCY; reported resolution: 3.1 Å). **b.** AAA+ ATPase, ClpL from *Streptococcus pneumoniae*: ATPPrS-bound (EMDB ID: 0967; PDB ID: 6LT4; reported resolution: 4.5 Å). **c.** Follicle stimulating hormone receptor (EMDB ID: 35136; PDB ID: 8I2H; reported resolution: 6 Å). Visualization of cryo-EM density maps and PDB structures was produced by UCSF ChimeraX [12].

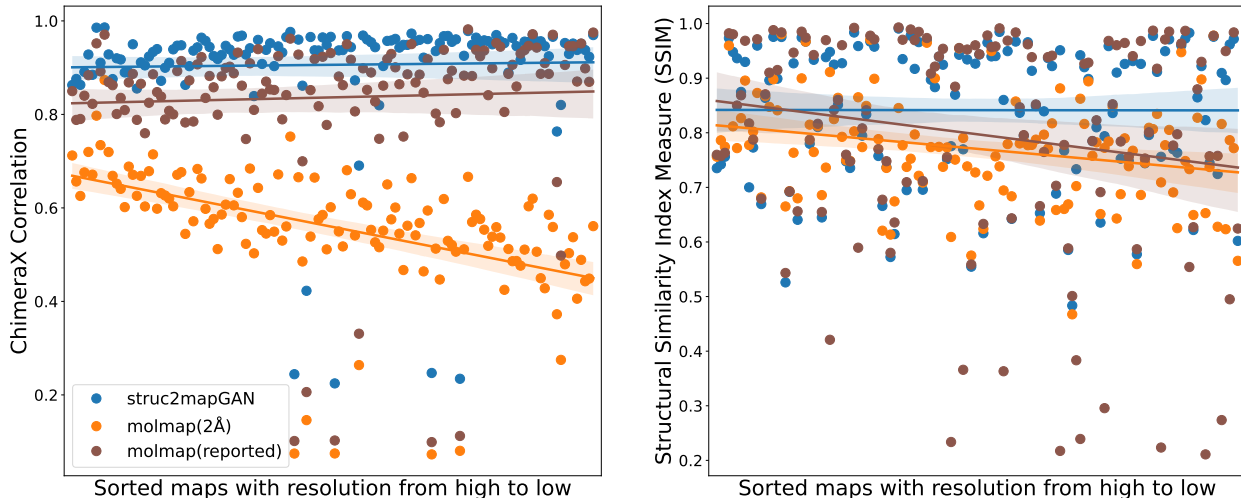


Figure 5: The scatter plots for comparison of ChimeraX correlation (left) and SSIM (right) for *struc2mapGAN* (blue dots), *molmap* at a resolution cutoff at 2 Å (orange dots), and *molmap* at the reported resolution cutoff (brown dots), across 130 test examples. The test examples were sorted by their reported resolutions from high to low. The shaded area around each colored regression line represents the confidence interval of the regression estimate.

4.5 Map generation time

To assess the potential use of *struc2mapGAN* in practice, we also recorded the time to generate experimental-like density maps from PDB structures for all 130 test examples. Figure 7 shows the wall-clock time plotted against the number of residues of each candidate structure. The scatter plot indicates that the relationship between the map generation time and the number of residues is approximately linear. Upon reviewing several instances, we found that it took around 14 and 20 seconds to generate maps containing 644 and 2501 residues, respectively. For a significantly larger structure with 12868 residues, the map generation time remained within an acceptable range, approximately 53 seconds. These results demonstrate that *struc2mapGAN* scales efficiently with the increasing complexity of protein structures, making it a viable tool for real-time applications.

5 Ablation study

Two key factors influence the learning efficiency of *struc2mapGAN*. The first is the incorporation of SmoothL1Loss in the generator as an additional constraint to mitigate mode collapse inherent in GANs and stabilize the training process. The second is the use of curated experimental maps as the learning targets, enabling the model to learn more accurate and reliable mappings between synthetic and experimental maps. To investigate the impact of these factors on the performance of *struc2mapGAN*, we trained two distinct GAN models: one without SmoothL1Loss (w/o L1) and the other using raw experimental maps without any curation. We then conducted these evaluations on both models using all 130 test examples. ChimeraX correlation scores are reported in Figure 8. The baseline *struc2mapGAN* (i.e. trained with SmoothL1Loss and using curated maps) achieved the highest mean and median scores, as well as the narrowest interquartile range. These results indicate that incorporating SmoothL1Loss enhances the preservation of overall similarity in the generated maps and leads to more consistent outcomes. Similarly, SSIM scores are reported in Figure 8, indicating slightly lower mean and median without SmoothL1Loss.

The model trained with only raw maps achieved SSIM scores with a mean of 0.842 and a median of 0.894, comparable to those of *struc2mapGAN* (mean of 0.841 and median of 0.896). This result was anticipated since the SSIM metric is more sensitive to local structural details. Training with raw maps maintained the local molecular information, resulting in minimal variance in SSIM scores. However, most noise, artifacts, and solvents were removed when raw maps were curated, which allows *struc2mapGAN* trained with these curated maps to focus more on overall similarity, thereby yielding higher correlation scores. These findings underscore the importance of using an additional SmoothL1Loss to guide network training and employing curated maps as input targets, both of which enhancing the model performance.

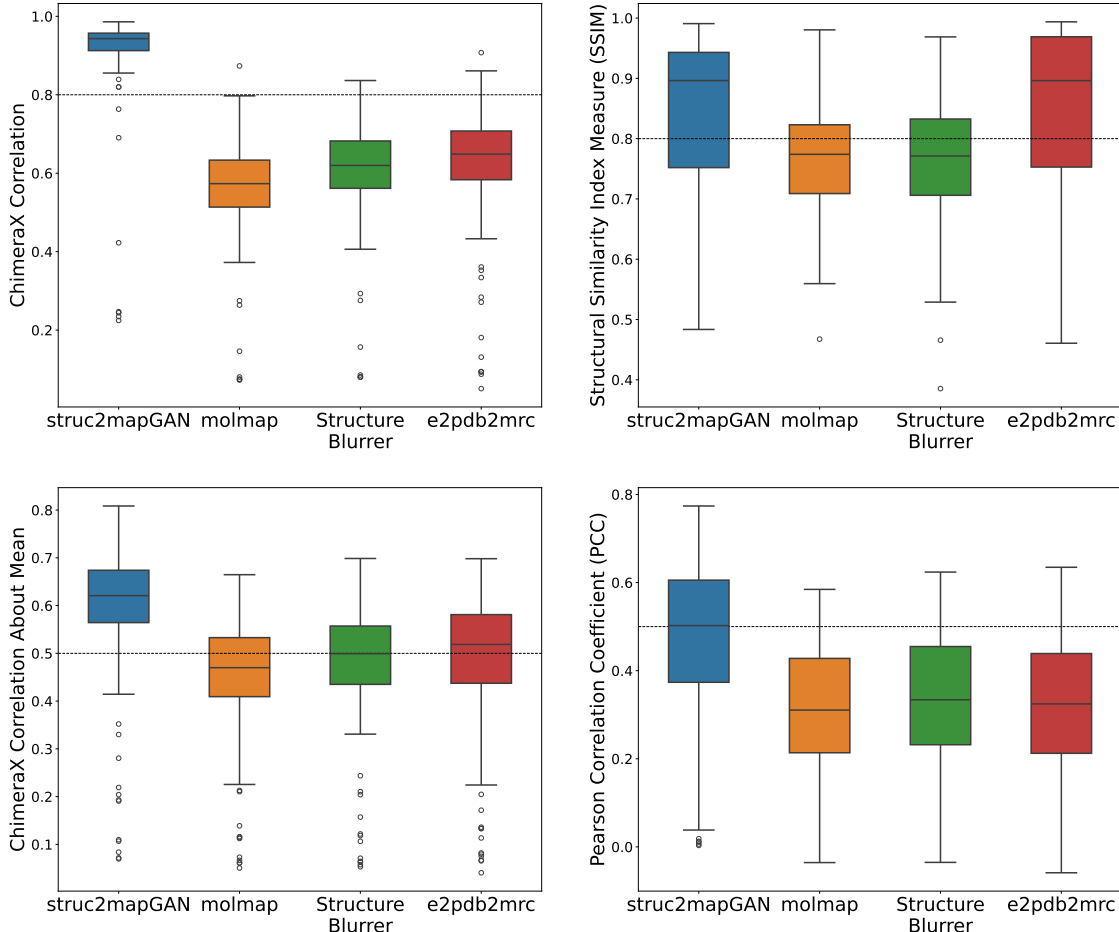


Figure 6: The box-whisker plots for comparison of different methods (*struc2mapGAN*, *molmap*, *StructureBlurrer*, and *e2pdb2map*) across four evaluation metrics over 130 test examples. For each box-whisker plot, the center line is the median; lower and upper hinges represent the first and third quartiles; the whiskers stretch to 1.5 times the interquartile range from the corresponding hinge; and the outliers are plotted as circles.

6 Discussion and conclusion

In this work, we present *struc2mapGAN*, a novel method adapted from the GAN architecture to generate cryo-EM density maps from PDB structures, which mimic the unique characteristics of raw maps. We enhance *struc2mapGAN*’s training efficiency by excluding the noise and artifacts and selectively extracting the macromolecule regions from the raw maps as training input, as well as incorporating SmoothL1Loss into the generator. Our benchmarking results show that *struc2mapGAN* outperforms existing simulation-based methods across various evaluation metrics. Moreover, its rapid synthesis speed makes it suitable for generating large-scale data.

Overall, by employing *struc2mapGAN*, structural biologists can synthesize improved experimental-like cryo-EM density maps in a timely manner, which can then be used for various applications, such as map-model validation, structure alignment, and guiding the particle-picking process during reconstruction of experimental maps. Furthermore, machine learning scientists can use *struc2mapGAN* to generate numerous experimental-like density maps as targets, enabling the re-training or fine-tuning of the existing models that were originally trained with simulation-based maps, thereby improving the model performance.

While our results demonstrate superior performance in generating improved density maps, it is not possible to relate these maps to an exact resolution value. In principle, it would be feasible to precisely modulate resolutions by integrating a resolution-conditioned modulation mechanism into the generator. This could involve conditioning the network on a continuous resolution parameter via learnable embedding layers or feature-wise linear modulation (FiLM) [33], allowing

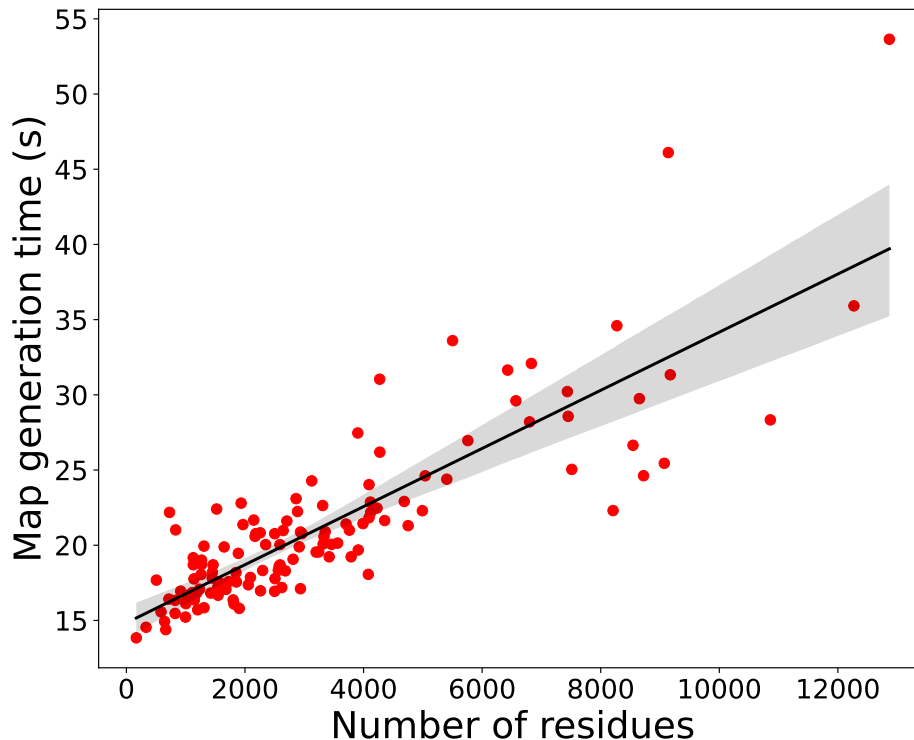


Figure 7: The scatter plot of map generation time against the number of residues in the molecule. Each red dot represents a molecule’s generation based on its residue count. The shaded area around the black regression line represents the confidence interval of the regression estimate. Running times were recorded for an AMD Ryzen Threadripper 2950X Processor with 32 CPUs.

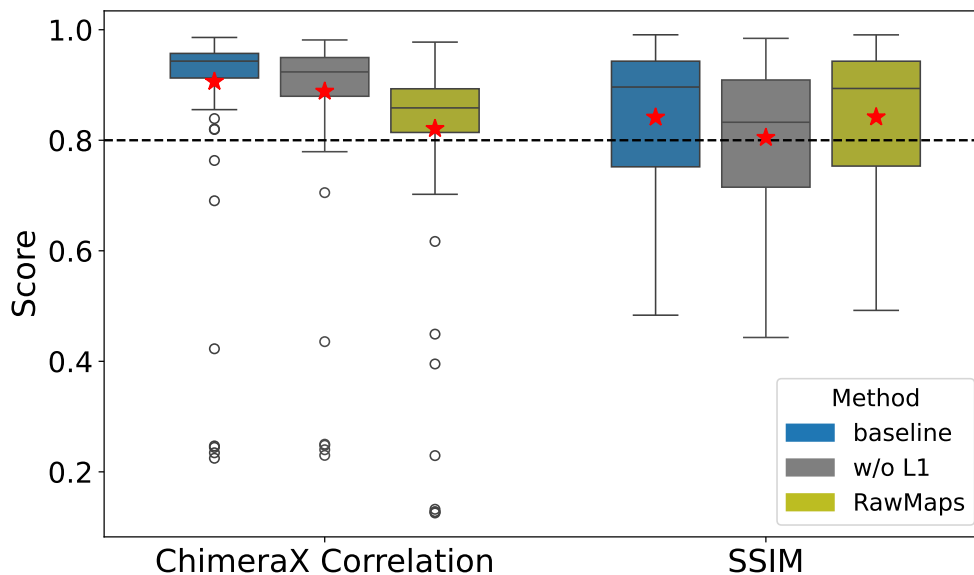


Figure 8: The box-whisker plots for comparison among *struc2mapGAN* (base), the network trained without SmoothL1Loss (w/o L1), and the network trained with uncurated raw experimental maps (RawMaps). The evaluation was made across two metrics: ChimeraX correlation and SSIM, based on 130 test examples. The red stars represent the mean values of corresponding scores.

explicit control over output resolution. Furthermore, with advancements in other generative models [34, 35], integrating attention modules into the generator of *struc2mapGAN* could enhance capturing detailed structural information from maps. It would also be interesting to utilize diffusion models for map generation. These will be left for our future work.

Interestingly, our method can also be employed to generate reliable density maps from structures predicted by AlphaFold [36] and other de novo sequence-to-structure generative methods [37, 38], serving as templates to guide and expedite the particle-picking process during the collection of cryo-EM 2D images for reconstructing experimental density maps [39, 40]. Moreover, these templates have the potential for template matching in cryo-electron tomography [41]. Exploring these applications will also be the focus of our future work.

Acknowledgments

This work is supported in parts by a NFRFE-2019-00486 grant.

Data Availability

The source code of *struc2mapGAN* is available on GitHub at <https://github.com/chenwei-zhang/struc2mapGAN>. The datasets were derived from sources in the public domain: EMDB databank [25] and PDB databank [26].

References

- [1] Jean-Paul Renaud, Ashwin Chari, Claudio Ciferri, Wen-ti Liu, Hervé-William Rémigy, Holger Stark, and Christian Wiesmann. Cryo-em in drug discovery: achievements, limitations and prospects. *Nature reviews Drug discovery*, 17(7):471–492, 2018.
- [2] Alan Merk, Alberto Bartesaghi, Soojay Banerjee, Veronica Falconieri, Prashant Rao, Mindy I Davis, Rajan Pragani, Matthew B Boxer, Lesley A Earl, Jacqueline LS Milne, et al. Breaking cryo-em resolution barriers to facilitate drug discovery. *Cell*, 165(7):1698–1707, 2016.
- [3] Kiarash Jamali, Lukas Käll, Rui Zhang, Alan Brown, Dari Kimanius, and Sjors HW Scheres. Automated model building and protein identification in cryo-em maps. *Nature*, pages 1–2, 2024.
- [4] Jonas Pfab, Nhut Minh Phan, and Dong Si. Deeptimizer for fast de novo cryo-em protein structure modeling and special studies on cov-related complexes. *Proceedings of the National Academy of Sciences*, 118(2):e2017525118, 2021.
- [5] Jiahua He, Peicong Lin, Ji Chen, Hong Cao, and Sheng-You Huang. Model building of protein complexes from intermediate-resolution cryo-em maps with deep learning-guided automatic assembly. *Nature Communications*, 13(1):4066, 2022.
- [6] Willy Wriggers and Jing He. Numerical geometry of map and model assessment. *Journal of structural biology*, 192(2):255–261, 2015.
- [7] Aryan Tajmir Riahi, Chenwei Zhang, James Chen, Anne Condon, and Khanh Dao Duc. Empot: partial alignment of density maps and rigid body fitting using unbalanced gromov-wasserstein divergence. *arXiv preprint arXiv:2311.00850*, 2023.
- [8] Steven J Ludtke, Philip R Baldwin, and Wah Chiu. Eman: semiautomated software for high-resolution single-particle reconstructions. *Journal of structural biology*, 128(1):82–97, 1999.
- [9] Jiahua He, Tao Li, and Sheng-You Huang. Improvement of cryo-em maps by simultaneous local and non-local deep learning. *Nature Communications*, 14(1):3217, 2023.
- [10] Xin Dai, Longlong Wu, Shinjae Yoo, and Qun Liu. Integrating alphafold and deep learning for atomistic interpretation of cryo-em maps. *Briefings in Bioinformatics*, 24(6):bbad405, 2023.
- [11] Guang Tang, Liwei Peng, Philip R Baldwin, Deepinder S Mann, Wen Jiang, Ian Rees, and Steven J Ludtke. Eman2: an extensible image processing suite for electron microscopy. *Journal of structural biology*, 157(1):38–46, 2007.
- [12] Eric F Pettersen, Thomas D Goddard, Conrad C Huang, Gregory S Couch, Daniel M Greenblatt, Elaine C Meng, and Thomas E Ferrin. Ucsf chimera—a visualization system for exploratory research and analysis. *Journal of computational chemistry*, 25(13):1605–1612, 2004.
- [13] Tristan Cragolini, Harpal Sahota, Agnel Praveen Joseph, Aaron Sweeney, Sony Malhotra, Daven Vasishtan, and Maya Topf. Tempy2: a python library with improved 3d electron microscopy density-fitting and validation workflows. *Acta Crystallographica Section D: Structural Biology*, 77(1):41–47, 2021.
- [14] Willy Wriggers. Conventions and workflows for using situs. *Acta Crystallographica Section D: Biological Crystallography*, 68(4):344–351, 2012.
- [15] Maytha Alshammari, Willy Wriggers, Jiangwen Sun, and Jing He. Refinement of alphafold2 models against experimental and hybrid cryo-em density maps. *QRB discovery*, 3:e16, 2022.
- [16] Zhaoyu Zhang, Mengyan Li, and Jun Yu. On the convergence and mode collapse of gan. In *SIGGRAPH Asia 2018 Technical Briefs*, pages 1–4. 2018.
- [17] Ron Bracewell and Peter B Kahn. The fourier transform and its applications. *American Journal of Physics*, 34(8):712–712, 1966.
- [18] Rafael C Gonzalez. *Digital image processing*. Pearson education india, 2009.
- [19] Antonia Creswell, Tom White, Vincent Dumoulin, Kai Arulkumaran, Biswa Sengupta, and Anil A Bharath. Generative adversarial networks: An overview. *IEEE signal processing magazine*, 35(1):53–65, 2018.
- [20] Jonas Adler and Sebastian Lunz. Banach wasserstein gan. *Advances in neural information processing systems*, 31, 2018.
- [21] Jun-Yan Zhu, Taesung Park, Phillip Isola, and Alexei A Efros. Unpaired image-to-image translation using cycle-consistent adversarial networks. In *Proceedings of the IEEE international conference on computer vision*, pages 2223–2232, 2017.

- [22] Harshit Gupta, Michael T McCann, Laurene Donati, and Michael Unser. Cryogan: A new reconstruction paradigm for single-particle cryo-em via deep adversarial learning. *IEEE Transactions on Computational Imaging*, 7:759–774, 2021.
- [23] Phillip Isola, Jun-Yan Zhu, Tinghui Zhou, and Alexei A Efros. Image-to-image translation with conditional adversarial networks. In *Proceedings of the IEEE conference on computer vision and pattern recognition*, pages 1125–1134, 2017.
- [24] Sai Raghavendra Maddhuri Venkata Subramaniya, Genki Terashi, and Daisuke Kihara. Enhancing cryo-em maps with 3d deep generative networks for assisting protein structure modeling. *Bioinformatics*, 39(8):btad494, 2023.
- [25] Catherine L Lawson, Ardan Patwardhan, Matthew L Baker, Corey Hryc, Eduardo Sanz Garcia, Brian P Hudson, Ingvar Lagerstedt, Steven J Ludtke, Grigore Pintilie, Raul Sala, et al. Emdatabank unified data resource for 3dem. *Nucleic acids research*, 44(D1):D396–D403, 2016.
- [26] Helen M Berman, Tammy Battistuz, Talapady N Bhat, Wolfgang F Bluhm, Philip E Bourne, Kyle Burkhardt, Zukang Feng, Gary L Gilliland, Lisa Iype, Shri Jain, et al. The protein data bank. *Acta Crystallographica Section D: Biological Crystallography*, 58(6):899–907, 2002.
- [27] Fernando Pérez-García, Rachel Sparks, and Sébastien Ourselin. Torchio: a python library for efficient loading, preprocessing, augmentation and patch-based sampling of medical images in deep learning. *Computer Methods and Programs in Biomedicine*, 208:106236, 2021.
- [28] Zongwei Zhou, Md Mahfuzur Rahman Siddiquee, Nima Tajbakhsh, and Jianming Liang. Unet++: A nested u-net architecture for medical image segmentation. In *Deep Learning in Medical Image Analysis and Multimodal Learning for Clinical Decision Support: 4th International Workshop, DLMIA 2018, and 8th International Workshop, ML-CDS 2018, Held in Conjunction with MICCAI 2018, Granada, Spain, September 20, 2018, Proceedings 4*, pages 3–11. Springer, 2018.
- [29] Dong Si, Spencer A Moritz, Jonas Pfab, Jie Hou, Renzhi Cao, Liguang Wang, Tianqi Wu, and Jianlin Cheng. Deep learning to predict protein backbone structure from high-resolution cryo-em density maps. *Scientific reports*, 10(1):4282, 2020.
- [30] Timothy Dozat. Incorporating nesterov momentum into adam. 2016.
- [31] Zhou Wang, Alan C Bovik, Hamid R Sheikh, and Eero P Simoncelli. Image quality assessment: from error visibility to structural similarity. *IEEE transactions on image processing*, 13(4):600–612, 2004.
- [32] Philip Sedgewick. Pearson’s correlation coefficient. *Bmj*, 345, 2012.
- [33] Ethan Perez, Florian Strub, Harm De Vries, Vincent Dumoulin, and Aaron Courville. Film: Visual reasoning with a general conditioning layer. In *Proceedings of the AAAI conference on artificial intelligence*, volume 32, 2018.
- [34] Ashish Vaswani, Noam Shazeer, Niki Parmar, Jakob Uszkoreit, Llion Jones, Aidan N Gomez, Łukasz Kaiser, and Illia Polosukhin. Attention is all you need. *Advances in neural information processing systems*, 30, 2017.
- [35] Jonathan Ho, Ajay Jain, and Pieter Abbeel. Denoising diffusion probabilistic models. *Advances in neural information processing systems*, 33:6840–6851, 2020.
- [36] John Jumper, Richard Evans, Alexander Pritzel, Tim Green, Michael Figurnov, Olaf Ronneberger, Kathryn Tunyasuvunakool, Russ Bates, Augustin Žídek, Anna Potapenko, et al. Highly accurate protein structure prediction with alphafold. *Nature*, 596(7873):583–589, 2021.
- [37] Minkyung Baek, Frank DiMaio, Ivan Anishchenko, Justas Dauparas, Sergey Ovchinnikov, Gyu Rie Lee, Jue Wang, Qian Cong, Lisa N Kinch, R Dustin Schaeffer, et al. Accurate prediction of protein structures and interactions using a three-track neural network. *Science*, 373(6557):871–876, 2021.
- [38] Zeming Lin, Halil Akin, Roshan Rao, Brian Hie, Zhongkai Zhu, Wenting Lu, Nikita Smetanin, Robert Verkuil, Ori Kabeli, Yaniv Shmueli, et al. Evolutionary-scale prediction of atomic-level protein structure with a language model. *Science*, 379(6637):1123–1130, 2023.
- [39] Yifan Cheng. Single-particle cryo-em—how did it get here and where will it go. *Science*, 361(6405):876–880, 2018.
- [40] Fred J Sigworth. Principles of cryo-em single-particle image processing. *Journal of Electron Microscopy*, 65(1):57–67, 2015.
- [41] Jochen Böhm, Achilleas S Frangakis, Reiner Hegerl, Stephan Nickell, Dieter Typke, and Wolfgang Baumeister. Toward detecting and identifying macromolecules in a cellular context: template matching applied to electron tomograms. *Proceedings of the National Academy of Sciences*, 97(26):14245–14250, 2000.

Table A1: List of all EMDB/PDB examples in training and validation sets. Examples in bold are used as the validation set.

EMDB	PDB	Resolution(Å)	EMDB	PDB	Resolution(Å)	EMDB	PDB	Resolution(Å)
26916	7UZQ	2.17	26617	7UN9	3.3	0310	6HZ4	3.6
26917	7UZS	2.2	34963	8HR8	3.3	6324	3JA7	3.6
26886	7UZE	2.4	0089	6GYB	3.3	9105	6ME0	3.6
26974	8CSX	2.4	0690	6J6K	3.3	9111	6MG8	3.6
26948	7V0Q	2.5	3297	5FTL	3.3	30346	7CFS	3.6
26949	7V0S	2.5	4571	6QK7	3.3	34738	8HGG	3.64
14774	7ZL1	2.5	6239	3J9D	3.3	15635	8AT6	3.7
15960	8BC2	2.6	6240	3J9E	3.3	0609	6O2N	3.7
33233	7XJP	2.71	6630	3JCZ	3.3	7041	6B3Q	3.7
27937	8E78	2.77	6932	5ZJI	3.3	8946	6E0F	3.7
27945	8E8O	2.77	6975	5ZK5	3.3	10099	6S59	3.7
26732	7USC	3	9390	6NJO	3.3	10399	6T8B	3.7
26733	7USD	3	10037	6RWB	3.3	20754	6UEN	3.7
26734	7USE	3	10836	6YLE	3.3	20857	6UR8	3.7
0785	6KZ4	3	21863	6WPK	3.3	0379	6N9U	3.7
9322	6N24	3	7006	6AUI	3.3	0688	6J6I	3.7
20442	6PPL	3	9898	6JZO	3.3	4650	6QVE	3.7
21149	6VCD	3	20583	6TYI	3.3	20651	6U5O	3.7
21366	6VRB	3	20968	6V03	3.3	30238	7BXU	3.7
30305	7C8D	3	0327	6I1Y	3.4	27645	8DQ0	3.74
30535	7DOI	3	0923	6LMX	3.4	28080	8EFD	3.8
6714	5XB1	3	0959	6LRR	3.4	28081	8EFE	3.8
21604	6WCA	3	9116	6MHQ	3.4	0935	6LO8	3.8
26838	7UWQ	3.05	9398	6NM9	3.4	7075	6BBJ	3.8
26978	8CT2	3.1	9887	6KUJ	3.4	9971	6KFF	3.8
0590	6O1K	3.1	9905	6K15	3.4	10401	6T8H	3.8
0784	6KZ3	3.1	9954	6KA4	3.4	20700	6U9H	3.8
9253	6MUR	3.1	10208	6SI8	3.4	20471	6PTJ	3.8
10539	6TNY	3.1	10232	6SKZ	3.4	0706	6KLC	3.9
22876	7KHA	3.1	21913	6WUH	3.4	7959	6DLZ	3.9
30016	6LYG	3.1	10206	6SI7	3.4	8185	5JZH	3.9
3999	6EZJ	3.1	33621	7Y5N	3.45	10893	6YS8	3.9
14716	7ZH0	3.2	26841	7UWS	3.47	4749	6R81	3.9
0936	6LOD	3.2	15673	8AUR	3.47	4917	6RLA	3.9
4789	6RB9	3.2	34430	8H1P	3.48	33719	7YAT	2.2
4907	6RKD	3.2	28666	8EY2	3.5	26973	8CSW	2.5
9653	6IFK	3.2	4581	6QLF	3.5	15361	8ADE	2.78
20650	6U5N	3.2	8750	5W0S	3.5	4798	6RBG	3
21146	6VBW	3.2	9104	6MDR	3.5	6941	5ZR1	3
21586	6WB8	3.2	9187	6MP6	3.5	15646	8ATD	3.1
30004	6LX3	3.2	10528	6TMV	3.5	4890	6RIE	3.1
30021	6LZ1	3.2	10573	6TT7	3.5	15540	8ANE	3.2
30022	6LZ3	3.2	20446	6PPR	3.5	6777	5XWY	3.2
30334	7CAL	3.2	20498	6PW4	3.5	0136	6H3N	3.3
0408	6NBD	3.2	20767	6UH5	3.5	8795	5WC3	3.5
5995	3J7H	3.2	22042	6X4S	3.5	0921	6LMV	3.6
20236	6P25	3.2	4746	6R7X	3.5	14725	7ZH6	3.67
20333	6PEV	3.2	21307	6VP9	3.5	4146	5M32	3.8
20334	6PEW	3.2	34679	8HDS	3.57	30005	6LXD	3.9
26616	7UN8	3.3	14873	7ZQP	3.6			

Table A2: List of all EMDB/PDB examples in the test set.

EMDB	PDB	Resolution(Å)	EMDB	PDB	Resolution(Å)	EMDB	PDB	Resolution(Å)
9590	6ACF	3	30180	7BTO	4	3602	5N8Y	4.7
22414	7JPK	3	6425	3JD6	4.1	6862	5YZ0	4.7
0199	6HCY	3.1	3835	5ONV	4.1	3439	5G5L	4.8
0927	6LN8	3.1	6746	5ZBO	4.1	6875	5Z1F	4.8
9321	6N23	3.1	6987	6A69	4.1	8665	5VFR	4.9
11093	6Z6G	3.1	7018	6AYE	4.1	8954	6E15	5.1
22829	7KDT	3.1	3866	6EGX	4.1	7322	6C05	5.2
0843	6L7E	3.2	4241	6FE8	4.1	3491	5MDX	5.3
9213	6MRU	3.2	4286	6FO0	4.1	9537	5GRS	5.4
0636	6O6R	3.2	4390	6GDG	4.1	4342	6G2D	5.4
20042	6OF4	3.2	9832	6JI1	4.1	8436	5TQW	5.6
10495	6TG9	3.2	0502	6NT5	4.1	10351	6SZA	6
10575	6TTF	3.2	5155	3IYJ	4.2	3885	6EL1	6.1
21481	6VZ1	3.2	3237	5FN2	4.2	8470	5TWV	6.3
10847	6YMX	3.2	3366	5G06	4.2	0608	6O2M	6.3
11488	6ZWM	3.2	4037	5LCW	4.2	1874	2Y9J	6.4
22359	7JK2	3.2	4112	5LVC	4.2	8230	5KBT	6.4
9361	6NFF	3.3	6734	5XMK	4.2	3636	5NG5	6.5
21458	6VYF	3.3	6859	5YYS	4.2	7065	6B7Y	6.5
22131	6XD3	3.3	6940	5ZQZ	4.2	5245	3IZI	6.7
30165	7BSS	3.3	4173	6F2D	4.2	5100	3IXV	6.8
9906	6K1H	3.5	0311	6HZ5	4.2	3761	5O8O	6.8
10213	6SJ7	3.5	20695	6U9E	4.2	6284	3J9T	6.9
20993	6V0C	3.5	8398	5TCP	4.3	3436	5G4F	7
21436	6VXF	3.5	6952	5ZSU	4.3	8097	5IOU	7
4339	6G1K	3.6	7476	6CHS	4.3	8187	5JZT	7.4
0775	6KSW	3.6	7793	6D3R	4.3	7461	6CE7	7.4
0836	6L53	3.6	8919	6DVW	4.3	8685	5VHW	7.8
30071	6M39	3.6	9214	6MRW	4.3	9949	6K9K	7.8
0043	6GOV	3.7	20524	6PYH	4.3	3186	5FJ6	7.9
0257	6HRA	3.7	10273	6SOF	4.3			
0567	6O0H	3.7	10549	6TQE	4.3			
10092	6S3K	3.7	30358	7CGN	4.3			
10214	6SJB	3.7	2364	4BTG	4.4			
21012	6V1I	3.8	6668	5H64	4.4			
10617	6XT9	3.8	8751	5W1R	4.4			
9626	6AHR	3.9	6911	5ZBG	4.4			
0071	6GVE	3.9	7967	6DMW	4.4			
9380	6NIL	3.9	0287	6HV8	4.4			
4537	6QEL	3.9	9870	6JPQ	4.4			
20708	6UAN	3.9	9915	6K4M	4.5			
7118	6BO4	4	0946	6LQI	4.5			
7464	6CES	4	0967	6LT4	4.5			
3984	6EZ8	4	30041	6M1D	4.5			
0088	6GY6	4	5917	4PT2	4.6			
0258	6HRB	4	3776	5OFO	4.6			
9883	6JTO	4	9577	6KV5	4.6			
9118	6MHU	4	22216	6XJX	4.6			
20265	6P6W	4	6535	3JC5	4.7			
20501	6PW9	4	2788	4V1W	4.7			